Production of very neutron-rich nuclei with a ^{76}Ge beam

O. B. Tarasov,[1,2,*] M. Portillo,[1] A. M. Amthor,[1,3] T. Baumann,[1] D. Bazin,[1] A. Gade,[1,3] T. N. Ginter,[1] M. Hausmann,[1] N. Inabe,[4]
T. Kubo,[4] D. J. Morrissey,[1,5] A. Nettleton,[1,3] J. Pereira,[1] B. M. Sherrill,[1,3] A. Stolz,[1] and M. Thoennessen[1,3]

[1]*National Superconducting Cyclotron Laboratory, Michigan State University, East Lansing, Michigan 48824, USA*
[2]*Flerov Laboratory of Nuclear Reactions, JINR, RU-141980 Dubna, Moscow Region, Russian Federation*
[3]*Department of Physics and Astronomy, Michigan State University, East Lansing, Michigan 48824, USA*
[4]*RIKEN Nishina Center, RIKEN, Wako-shi, Saitama 351-0198, Japan*
[5]*Department of Chemistry, Michigan State University, East Lansing, Michigan 48824, USA*

Production cross sections for neutron-rich nuclei from the fragmentation of a ^{76}Ge beam at 132 MeV/u were measured. The longitudinal momentum distributions of 34 neutron-rich isotopes of elements $13 \leqslant Z \leqslant 27$ were scanned using a novel experimental approach of varying the target thickness. Production cross sections with beryllium and tungsten targets were determined for a large number of nuclei, including 15 isotopes first observed in this work. These are the most neutron-rich nuclides of the elements $17 \leqslant Z \leqslant 25$ (^{50}Cl, ^{53}Ar, ^{55,56}K, ^{57,58}Ca, ^{59,60,61}Sc, ^{62,63}Ti, ^{65,66}V, ^{68}Cr, and ^{70}Mn). A one-body Q_g systematics is used to describe the production cross sections based on thermal evaporation from excited prefragments. Some of the fragments near ^{58}Ca show anomalously large production cross sections.

I. INTRODUCTION

The discovery of new nuclei in the proximity of the neutron drip line provides a benchmark for nuclear mass models and hence for the understanding of the nuclear force and the creation of elements. Once the production methods and cross sections for the formation of neutron-rich nuclei are understood, further investigations to study the nuclei themselves, such as decay spectroscopy, may be planned. Therefore, the determination of production rates for the most exotic nuclei continues to be an important part of the experimental program at existing and future rare-isotope facilities.

A number of production mechanisms have been used to produce neutron-rich isotopes for $17 \leqslant Z \leqslant 25$. For example, ^{57,58}V were observed for the first time in deep-inelastic reactions in 1980 [1], ^{59,60}V [2] and ^{61}V [3] by fragmentation of a ^{86}Kr beam for the first time in 1985 and 1992, respectively, and ^{62,63,64}V were first observed as products of projectile fission in 1997 [4]. The on-line isotope separation technique was used to produce for the first time ^{53,54}K and ^{53}Ca in 1983 [5], and 14 years later, ^{54,55,56}Ca isotopes were observed following in-flight fission of ^{238}U [4]. The possibility of producing very neutron-rich isotopes (e.g., ^{58,60}Ca) in transfer-type reactions at intermediate beam energies has been discussed recently [6].

New progress in the production of neutron-rich isotopes is possible given the increased primary beam intensities at the National Superconducting Cyclotron Laboratory (NSCL) at Michigan State University, and advances in experimental techniques [7] allowed probing further into unknown regions of the table of the isotopes with fragmentation reactions. Indeed, recent measurements at the NSCL [7–9] have demonstrated

that the fragmentation of ^{48}Ca and ^{76}Ge beams can be used to produce new isotopes in the proximity of the neutron drip line. Continuing this work, we report here the next step toward the fundamental goal of defining the absolute mass limit for chemical elements in the region of calcium.

The search for new neutron-rich isotopes was carried out with a primary beam of ^{76}Ge and using the two-stage fragment separator technique that enabled the discovery of ^{40}Mg and ^{42}Al in 2007 [7]. In the present measurement, 15 neutron-rich isotopes with $33 \leqslant N \leqslant 45$ were identified for the first time (see Fig. 1) and indications for the existence of a new island of inversion centered on ^{62}Ti—as predicted by Brown [11]—were described in a previous brief presentation of this work [12]. In this paper, we describe the details of our experimental approach and discuss the results.

II. EXPERIMENTAL DETAILS

A. Setup

A 132 MeV/u ^{76}Ge beam, accelerated by the coupled cyclotrons at the NSCL, was used to irradiate a series of beryllium targets and a tungsten target, each placed at the target position of the A1900 fragment separator [13]. Previous studies [8] demonstrated that using the A1900 fragment separator as the sole separation stage significantly limits the sensitivity of the experimental setup for very rare isotopes owing to

(i) excessive rates and large pile-up probability in the detector located at the intermediate dispersive focal plane of the A1900 fragment separator (required to measure the momentum) and

(ii) high rates of light nuclei in the final focal plane detectors that cannot be rejected by the energy-loss technique.
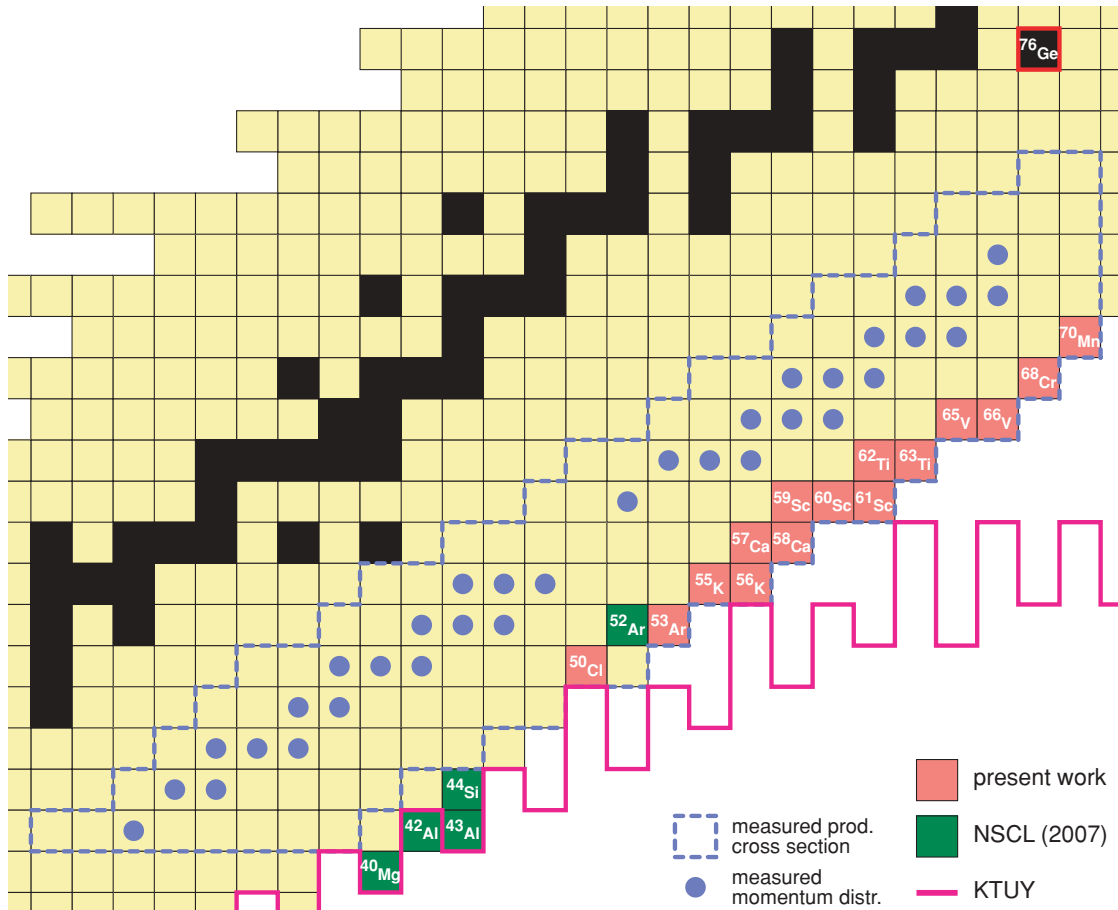
_____
*tarasov@nscl.msu.edu

FIG. 1. (Color online) The region of the nuclear chart investigated in the present work. The solid line shows the limit of bound nuclei from the KTUY mass model [10]. The 15 new isotopes observed for the first time in the present work are marked by red squares.

The combination of the A1900 fragment separator with the S800 analysis beam line [14] to form a two-stage separator system, as described in Ref. [7], allows a high degree of rejection of unwanted reaction products so that the full primary beam intensity can be utilized, while preserving the unambiguous identification of single exotic ions. The first stage of the system serves as a selector whereas the second stage contains detectors and functions as analyzer (see Fig. 2).

In the present work the momentum acceptance of the A1900 was varied from $\Delta p/p = 0.1\%$ to 5%. For all settings, the horizontal and vertical angular acceptances were ± 65 and ± 40 mrad. At the end of the S800 analysis beam line, the particles of interest were stopped in a telescope of eight silicon PIN diodes (50×50 mm^2) with a total thickness of 8.0 mm. This provided multiple energy-loss measurements and thus a redundant determination of the nuclear charge of each fragment in addition to the total kinetic energy. A 5-cm-thick plastic scintillator positioned behind the Si telescope served as a veto detector against reactions in the Si telescope and provided a measurement of the residual energy of lighter ions that were not stopped in the Si telescope. A position-sensitive parallel-plate avalanche counter (PPAC) was located in front of the Si telescope. This position measurement allowed for an additional discrimination against various scattered particles.

The primary ^{76}Ge^{30+} beam current was continuously monitored by a BaF$_2$ crystal mounted on a photomultiplier tube near the target position, as well as a nonintercepting capacitive pickup before the target. These indirect monitors were normalized to Faraday cup readings throughout the course of the experiment. The average beam intensity for the measurements of the most exotic fragments was approximately $1\ e\ \mu$A.

The time of flight (TOF) of each particle that reached the detector stack was measured in four different ways (see Table I). All TOF signals were used for the rejection of unwanted events. The first three TOF measurements listed

TABLE I. Flight paths between various timing detectors.

No.	Timing signals between		Length (m)
1	FP scintillator	Second PIN detector	46.0
2	OBJ scintillator	Third PIN detector	21.0
3	FP scintillator	OBJ scintillator	25.1
4	Target[a]	Third PIN detector	81.5

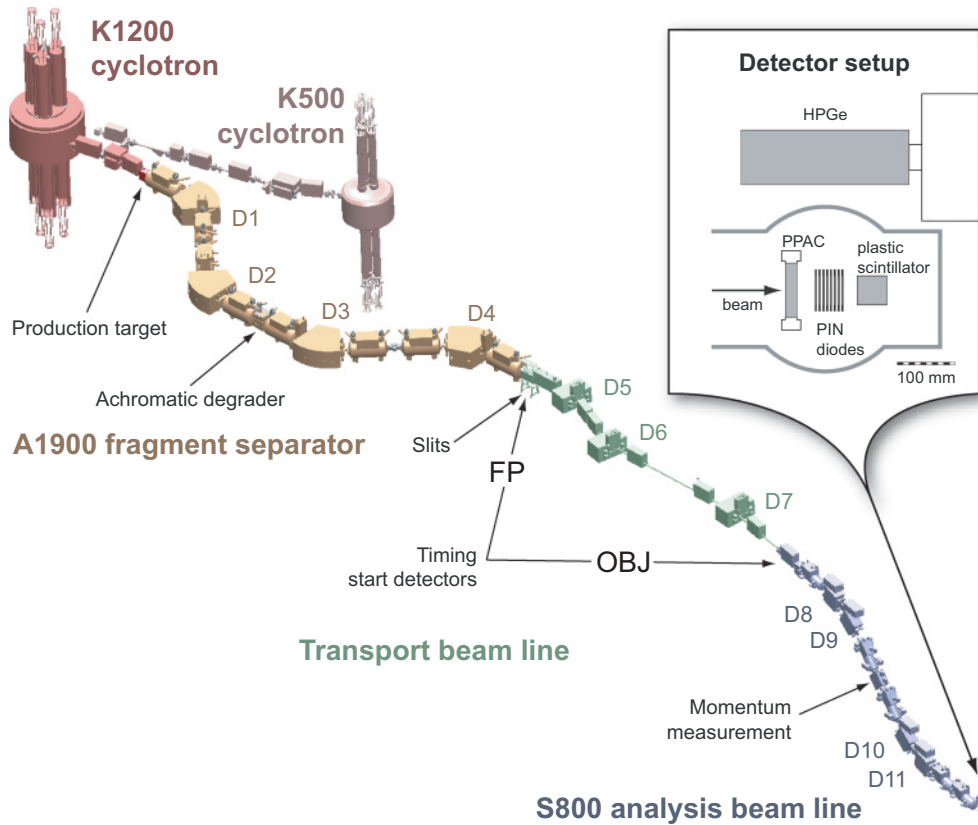[a]From the arrival time relative to the phase of the cyclotron rf signal.

FIG. 2. (Color online) Sketch of the experimental setup at the NSCL. This overview diagram shows the equipment used for the production, separation, and detection of new neutron-rich nuclei.

in the table were used to deduce the mass-to-charge ratio A/q with a better resolution than with a single TOF measurement.

The magnetic rigidity $(B\rho)$ of each particle was obtained by combining position measurements from two PPACs located in the dispersive plane of the S800 analysis beam line with NMR measurements of the dipole fields.

The simultaneous measurement of multiple ΔE signals, the magnetic rigidity, the total energy, and the TOFs of each particle provided an unambiguous identification of the atomic number, charge state, and mass number of each ion. The detection system and particle identification was calibrated with the primary beam and confirmed by the locations of gaps corresponding to unbound nuclei in the particle identification spectrum. In addition, a germanium γ-ray detector was placed near the Si telescope (see Fig. 2) to provide an independent verification of the isotope identification via isomer tagging, as described in Ref. [15].

B. Experimental runs

The present experiment consisted of three parts, which are summarized in Table II. During all runs, the magnetic rigidity of the last two dipoles was kept constant at 4.3 Tm while the production target thickness was changed to map the fragment momentum distributions. This approach greatly simplified the particle identification during the scans of the parallel momentum distributions.

The momentum acceptance of the A1900 fragment separator was restricted to $\Delta p/p = 0.1\%$ for the first part of the experiment devoted to the measurement of differential momentum distributions. The use of different beryllium target thicknesses (9.8, 97.5, 191, 288, and 404 mg/cm^2) allowed coverage of the different spans of the fragment momentum distributions necessary to extract production cross sections and also resulted in more isotopes in the particle identification spectrum. The particle selection depends critically on the magnetic rigidity of the fragment separator because the average energy (and therefore the magnetic rigidity) of a given reaction product decreases with increasing target thickness. As a result, the isotopic selection of this system moved toward more neutron-rich fragments with increasing target thickness.

For the second part of the experiment, a Kapton wedge with a thickness of 20.2 mg/cm^2 (indicated as an achromatic degrader in Fig. 2) was used at the dispersive image of the A1900 to reject less exotic fragments with an 8-mm aperture in the focal plane while the separator was set for ^{43}S. The goal of this setting was to confirm the particle identification by isomer tagging with ^{43m}S ($E_\gamma = 319$ keV, $T_{1/2} = 0.48$ μs) and ^{32m}Al ($E_\gamma = 735$ keV, $T_{1/2} = 0.2$ μs).

In the final part of the experiment, dedicated to the search for the new isotopes, four settings were used to cover the most neutron-rich isotopes with $13 \leqslant Z \leqslant 27$, as it is impossible to find a single target thickness and magnetic rigidity to produce all of the fragments of interest. Each setting was characterized

TABLE II. Experimental settings.

Data set	Fragment of interest	Magnetic rigidity, $B\rho$ (Tm)					Target (mg/cm^2)	Stripper (mg/cm^2)	Wedge (mg/cm^2)	$\Delta p/p$ (%)	Time (h)	Beam particles	Goal
		$D_1 D_2$	$D_3 D_4$	$D_5 D_6 D_7$	$D_8 D_9$	$D_{10} D_{11}$							
1	^{43}S	4.3233	4.3233	4.3134	4.3036	4.3000	Be 9.8	–	–	0.1	0.98	1.41×10^{14}	
2							Be 97.5	–	–	0.1	2.03	1.50×10^{14}	momentum
3							Be 191	–	–	0.1	1.98	2.07×10^{14}	distribution
4							Be 288	–	–	0.1	1.85	1.17×10^{14}	
5							Be 404	–	–	0.1	0.94	5.76×10^{13}	
6	^{43}S	4.3372	4.3233	4.3134	4.3036	4.3000	Be 191	–	20.2	1	3.36	1.25×10^{15}	^{43m}S
7							Be 288	–	20.2	2	5.97	1.96×10^{15}	production
8	^{66}V	4.3609	4.3383	4.3222	4.3059	4.3000	Be 404	–	20.2	5	19.86	1.42×10^{16}	
9							W 567	C 12	20.2	5	20.74	1.47×10^{16}	production
10	^{54}Ar	4.3529	4.3332	4.3192	4.3051	4.3000	W 567	Be 145	20.2	5	10.33	7.55×10^{15}	of new
11							Be 629	–	20.2	5	9.37	6.15×10^{15}	isotopes
12	^{59}Ca	4.3566	4.3355	4.3205	4.3054	4.3000	Be 629	–	20.2	5	21.60	1.58×10^{16}	
13	^{58}Ca	4.3546	4.3342	4.3198	4.3052	4.3000	W 567	Be 97.5	20.2	5	46.59	3.34×10^{16}	

by a fragment on which the separator was tuned. A search for the most exotic nuclei in each setting was carried out with Be and W targets. The four settings were centered on ^{54}Ar, ^{58,59}Ca, and ^{66}V, respectively, and were based on LISE^{++} [16] calculations using the parametrizations of the momentum distributions obtained in the first part of experiment (see Sec. IV A). The momentum acceptance of the A1900 was set to the maximum of $\Delta p/p = 5.0\%$ for these production runs. In contrast to previous studies with the A1900 as single-stage separator (e.g., Ref. [8]), the present overall experimental efficiency was dominated by the acceptance of the two-stage separator and not by the limitations from high counting rates of unwanted nuclei.

III. ANALYSIS OF EXPERIMENTAL DATA

The advantage of our approach—keeping the magnetic rigidity ($B\rho_{0f}$) constant while varying the target thickness—can be seen in Fig. 3, which shows the total distribution of fully stripped reaction products observed in all runs of this work. The range of fragments is shown as the measured atomic number Z plotted versus the calculated quantity $A - 3q$. The identification of the individual isotopes in Fig. 3 was confirmed via isomer tagging using the known isomeric decays in ^{32}Al and ^{43}S and from holes in the $A - 3Z = 1$ line corresponding to the unbound nuclei ^{25}O and ^{28}F located between the particle bound nuclei ^{22}N and ^{31}Ne. The details of the calculation of the particle identification are given in the Appendix.

The ionic (q) and elemental (Z) spectra obtained for particles that stopped in the Si telescope are shown in Fig. 4. The peaks were fitted with Gaussian distributions of constant width. The standard deviations were found to be $\sigma_q = 0.073$ for the ionic spectrum and $\sigma_Z = 0.098$ for the elemental spectrum, respectively. This means that the probabilities of one event being misidentified as a neighboring charge state or element are equal to $P_q(0.5) = 3.7 \times 10^{-12}$ and $P_Z(0.5) = 1.7 \times 10^{-7}$, respectively.
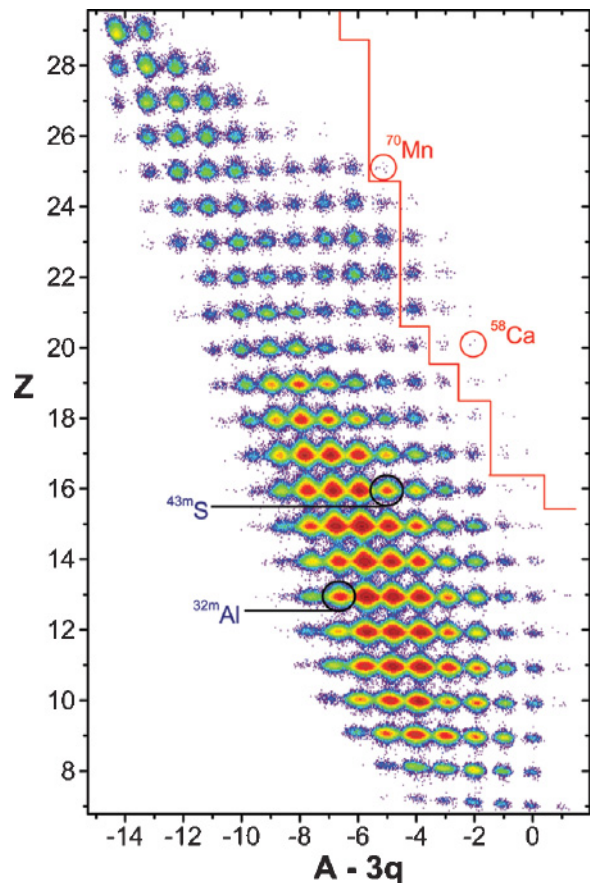

FIG. 3. (Color online) Particle identification plot showing the measured atomic number Z vs the calculated function $A - 3q$ for the nuclei observed in this work (where q is the ionic charge of the fragment). See text for details. The limit of previously observed nuclei is shown by the solid line as well as the locations of several reference nuclei. Particle identification was confirmed by registering γ rays from short-lived isomeric states of ^{43}S and ^{32}Al (marked by black circles).
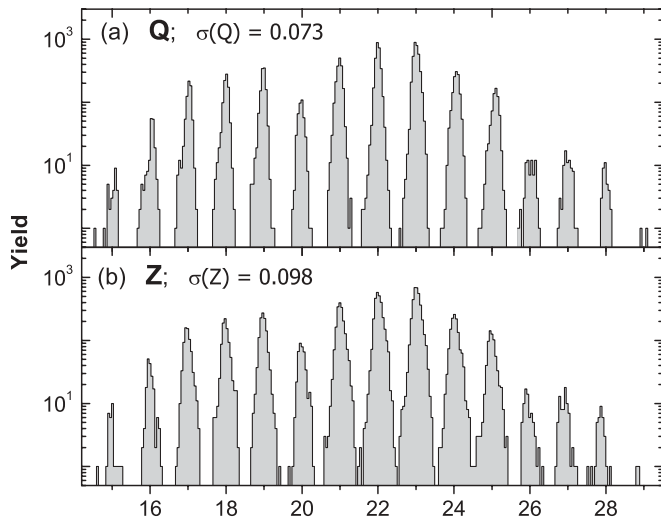
FIG. 4. Ionic (a) and elemental (b) spectra obtained with Eq. (A3) and (A5) for all particles stopped in the Si telescope during the data set dedicated to the search for new isotopes (see Table II).

The mass spectra for the isotopic chains from chlorine to manganese measured during the production runs are shown in Fig. 5. Only nuclei that stopped in the Si detector stack

are included in this analysis. The observed fragments include 15 new isotopes that are the most neutron-rich nuclides yet observed of elements $17 \leqslant Z \leqslant 25$ (^{50}Cl, ^{53}Ar, ^{55,56}K, ^{57,58}Ca, ^{59,60,61}Sc, ^{62,63}Ti, ^{65,66}V, ^{68}Cr, and ^{70}Mn). The new neutron-rich nuclei observed in this work are those events to the right of the solid line in Fig. 3 and to the right of the vertical dashed lines in Fig. 5. As noted before [12], the previously reported observation of ^{51}Cl [17] may have actually been an observation of the hydrogen-like charge state ^{48}Cl^{16+}.

IV. RESULTS AND DISCUSSION

A. Parallel momentum distributions

It is important to be able to predict the momentum distributions of residues when searching for new isotopes to optimize the fragment separator at the maximum production rate. Also, the accurate prediction of the momentum distributions allows estimation of the transmission and efficient rejection of strong contaminants. Several studies of the parallel momentum distributions have been made (e.g., Refs. [18–21]), but the predictions for the production of the most exotic nuclei are still very uncertain. In the few semiempirical models [18,19] used to describe the data Gaussian momentum distributions are
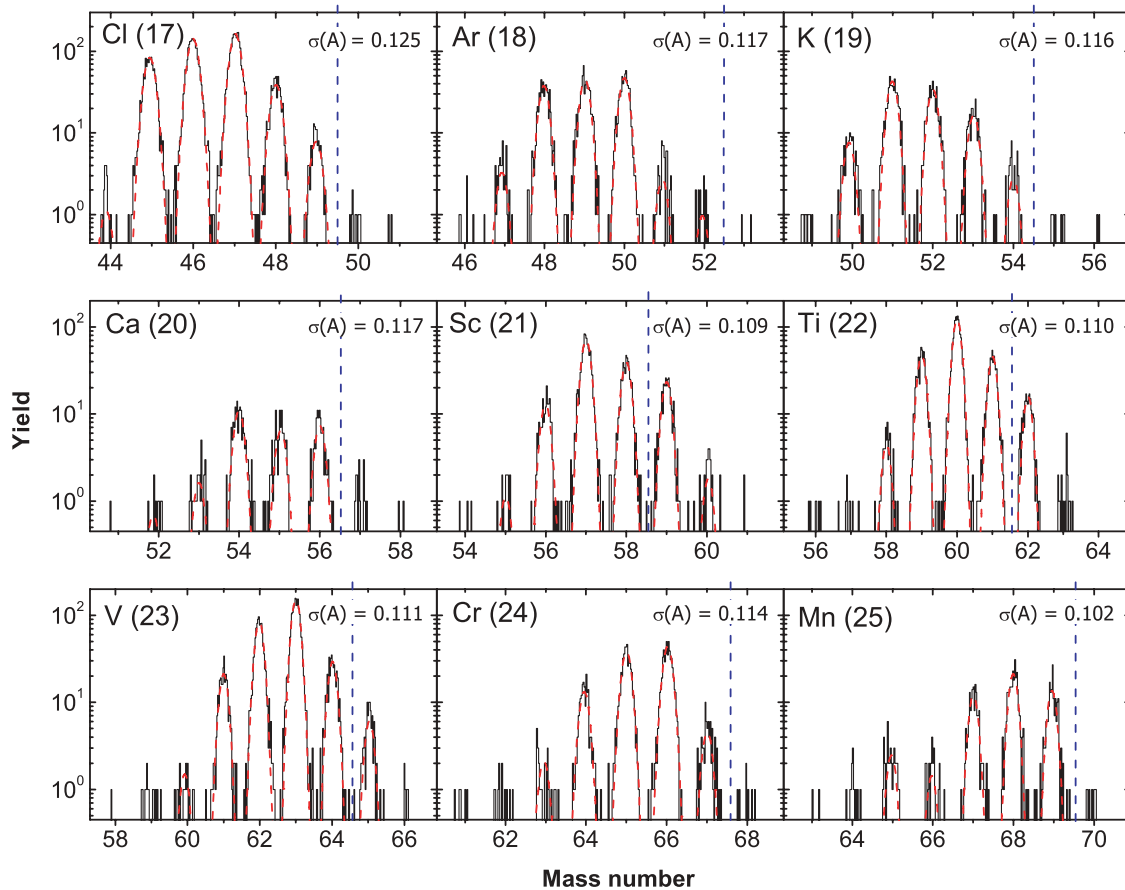

FIG. 5. (Color online) Mass spectra of the elements $17 \leqslant Z \leqslant 25$. All particles that were stopped in the Si telescope during the production runs were analyzed. The limits of previously observed nuclei are shown by the vertical dashed lines. Standard deviations produced in multipeak fits with Gaussian distributions at constant width (red dashed curves) are shown in the plots for each element.
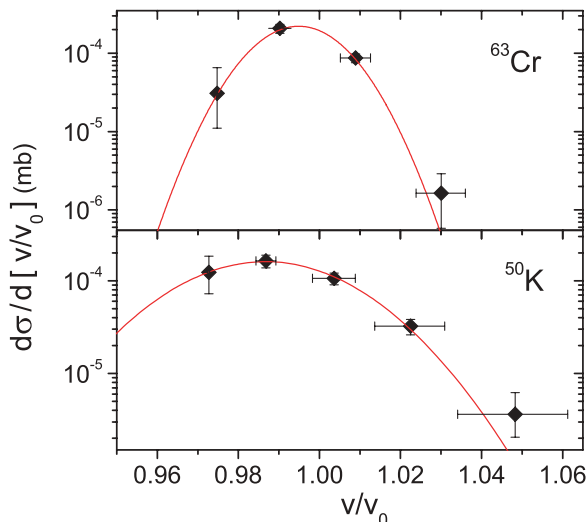
FIG. 6. (Color online) Differential cross sections of ^{63}Cr (top) and ^{50}K (bottom) fragments obtained by varying the target thickness at one magnetic rigidity. Red solid lines represent the fitted Gaussian functions. Horizontal errors correspond to the velocity difference caused by production at the beginning or the end of the target.

assumed, these are characterized just by two parameters (the mean value and the width) that may not be sufficient to model the momentum distributions. Therefore, the measurement of the fragment momentum distributions remains an important part of the search for new isotopes.

The most straightforward and common way to measure the momentum distributions of projectile fragments is to scan the magnetic rigidity of the fragment separator. A thin target is generally used for this measurement to avoid complications from differential energy loss in the target (the systematic change in the kinetic energy lost by the beam nucleus and product nuclei in the target). In addition, the momentum acceptance of the fragment separator is often restricted to a small value for isotopes with large yields. The acceptance is then opened up for the smaller yields, producing fewer measurements with larger systematic uncertainties. The total cross section is determined by integrating these momentum distributions by using some estimate, or measurement, of the angular transmission (e.g., Ref. [22]).

In the present work a new approach to measure momentum distributions and cross sections was used. In contrast to the "$B\rho$ scanning" method using one thin target, a variety of targets with different thicknesses were used at constant magnetic rigidity. This method is particularly well suited to survey neutron-rich nuclei since the less exotic nuclei are produced with the highest yields and their momentum distributions can be measured with the thin targets. The lighter fragments with high yields will experience the largest differential energy losses and will fall outside the constant momentum acceptance of the separator with the thicker targets. Conversely, the heaviest fragments with the lowest yields will only be produced in sufficient numbers in the thickest targets and will have lower differential energy losses. Extensive simulations of the A1900/S800 tandem separator showed that this method

can provide a sensitive measurement of the mean value and width of the momentum distribution [23]. However, as in the $B\rho$ scanning method, the momentum distributions of some fragments will be incomplete.

Five targets were used to measure the momentum distributions (see Table II). The yields of two example fragments, ^{63}Cr and ^{50}K, shown in Fig. 6 as a function of reduced velocity, were fitted with Gaussian functions and the total production cross sections were inferred. The momentum distributions for 34 isotopes were derived (indicated by the bullets in Fig. 1) and integrated to deduce the cross sections. It should be noted that at the energy of these experiments, the shape of the fragment momentum distribution is asymmetric because of a low-energy exponential tail stemming from dissipative processes [21]. The Gaussian function used for the present data does not take this tail into account, but the underestimation of the cross section is small. As one example, the ^{58}Ca cross section is underestimated by approximately 2%.

A survey of all of the fitted results showed that fragments in the heavy-mass region were produced with significantly higher velocities and slightly broader momentum distributions than the model predictions. In the model [19] used for these calculations it is assumed that the energy necessary to remove each nucleon is $E_S = 8$ MeV, a value derived for fragments close to stability. Further analysis showed that the separation energy parameter for nuclei observed in the present work in the region $A_P/2 \leqslant A_F \leqslant A_P$ exhibits a linear decrease with the number of removed nucleons:

$$E_S = 8 - 11.2\Delta A/A_P, \tag{1}$$

where $\Delta A = A_P - A_F$, A_P is the projectile mass number, and A_F is the fragment mass number.

The measured yields of the two example isotopes, ^{63}Cr and ^{50}K, are shown as a function of target thickness in Fig. 7. The fragment yields calculated with the LISE^{++} code [16] using parameters from Morrissey's model of the reaction with EPAX cross sections [24] are shown by the dashed lines. The fragment yields from the same calculations with the experimental parameters from fitting the velocity distributions (see Fig. 6) are shown by the solid lines in Fig. 7. Only a fair agreement is found with the model calculations with default settings. However, the agreement between experimental data and model calculations with parameters produced by fitting the velocity distributions is excellent and gives confidence that the fragment separator was set to optimize the yield of the weakest, most neutron-rich fragments.

B. Production cross section

The inclusive production cross sections for the observed fragments were calculated by correcting the measured yields for the finite longitudinal and angular acceptances of the separator system. A total of 34 cross sections with beryllium were obtained from Gaussian functions fitted to the longitudinal momentum distributions; these nuclei are indicated by stars in Fig. 8. The cross sections for all of the remaining fragments with incomplete longitudinal momentum distributions were obtained with estimated transmission corrections.
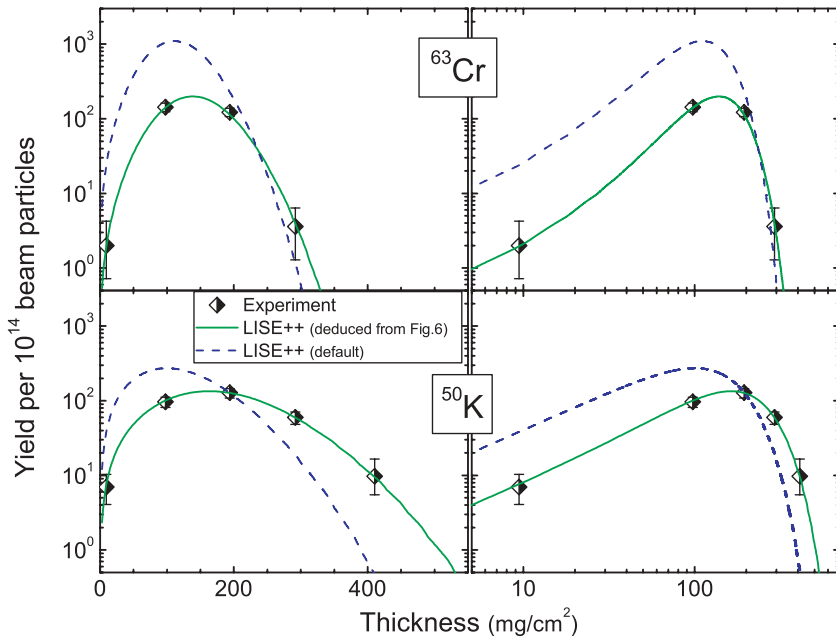
FIG. 7. (Color online) The measured yield of ^{63}Cr (top) and ^{50}K (bottom) as a function of target thickness. The lines show the LISE^{++} calculations with results of fitting the velocity distributions shown in Fig. 6 (green solid line) and default model settings [19] (blue dashed line) as described in the text. Note that the left panels have linear horizontal scales, whereas the right panels have logarithmic scales to emphasize the difference between calculated curves for the thick and thin targets.

The angular and longitudinal transmissions were calculated for each isotope in each setting using a model of the momentum distribution with smoothly varying parameters extracted from the measured parallel momentum distributions. For example, the values of the angular, momentum, and overall transmissions, as well as the wedge selection for the central
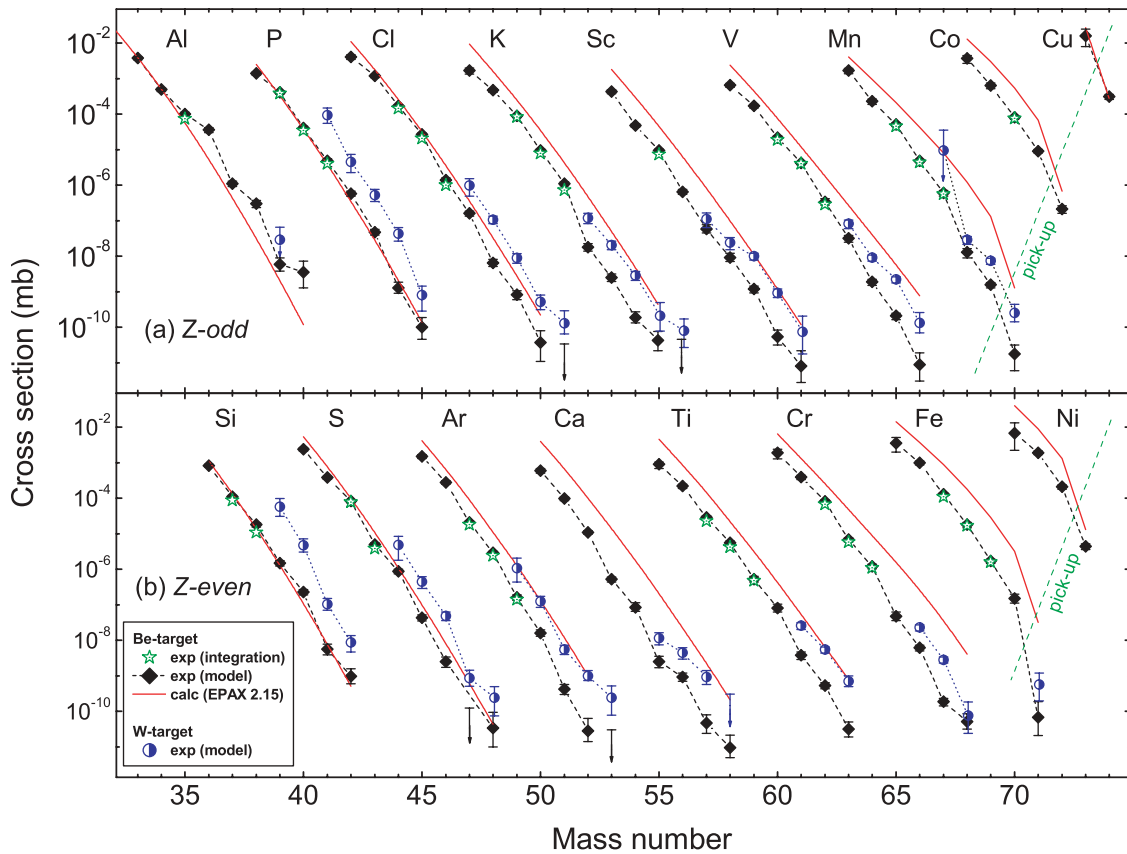

FIG. 8. (Color online) Inclusive production cross sections for fragments from the reaction of ^{76}Ge with beryllium and tungsten targets shown as a function of mass number. The cross sections derived with the beryllium targets are shown by stars; those normalized with LISE^{++} transmission calculations are indicated by solid diamonds. The cross sections obtained with the tungsten target were normalized with LISE^{++} transmission calculations. The two green dashed lines separate nuclei that require neutron pickup in the production mechanism. The red lines show the predictions of the EPAX systematics for beryllium (see text).

TABLE III. Transmissions during runs with a wedge.

Data set	Fragment of interest	Transmission (%)			
		Momentum	Angular	Wedge selection	Total
6	^{43}S	11 ± 3	70^{+7}_{-8}	75^{+10}_{-14}	6 ± 2
7	^{43}S	16 ± 3	69^{+7}_{-8}	74^{+10}_{-14}	8 ± 2
8	^{66}V	70 ± 3	99^{+1}_{-2}	83^{+8}_{-13}	58^{+6}_{-10}
9	^{66}V	69 ± 3	99^{+1}_{-2}	83^{+9}_{-13}	56^{+6}_{-9}
10	^{54}Ar	47 ± 6	88^{+4}_{-6}	79^{+9}_{-14}	33^{+6}_{-8}
11	^{54}Ar	30 ± 3	86^{+7}_{-6}	78^{+10}_{-14}	20^{+3}_{-4}
12	^{59}Ca	32 ± 3	93^{+3}_{-5}	80^{+9}_{-14}	24^{+3}_{-5}
13	^{58}Ca	41^{+2}_{-1}	93^{+3}_{-5}	80^{+9}_{-14}	31^{+4}_{-6}

fragment in runs with a wedge, are given in Table III. The wedge selection represents the fraction of isotopes that passed through the slits at the focal plane when the wedge is inserted at the intermediate dispersive image. The estimate of the uncertainties in the transmissions came from the values at the one-sigma limits of the reduced width of the longitudinal momentum distributions scaled by the mass loss [19]:

$$\sigma_{||} = \sigma_0 \sqrt{\Delta A}, \qquad (2)$$

where ΔA was defined earlier and $\sigma_0 = 105 \pm 15$ MeV/c. Details of transmission calculations, the analysis of their uncertainties, as well as the general analysis of momentum distributions taken from various target thicknesses will be described in a subsequent paper [23].

The cross sections obtained for all of the fragments observed in this experiment are shown in Fig. 8 along with the predictions of the EPAX parametrization. The systematic errors associated with the target thickness, beam current measurements, and the widths of the momentum slits have been included in the error bars and were 11% for the first data set and approximately 2% for production data sets (8–13). For those isotopes that relied on transmission calculations, the weighted mean of all measured yields was used to obtain the "model-based" cross section (shown by solid diamonds in Fig. 8). The uncertainties in these cases included statistical, systematic, and transmission uncertainties. As can be seen in Fig. 8, the model-based cross sections are in good agreement with those produced by integrating the measured longitudinal momentum distributions, as was shown earlier for the examples ^{63}Cr and ^{50}K.

The runs with the tungsten target employed stripper foils (Be and C) placed directly behind the target, which should be taken into account for the determination of the cross sections. Such a correction can easily be made for the most neutron-rich isotopes (for example $^{59-61}$Sc) for which the ratio of the observed cross sections $R = \sigma_W/\sigma_{Be}$ exceeds ≈ 10. Cross sections with the tungsten target for isotopes with $R \approx 1$ can be reliably obtained if the corresponding cross section with the beryllium target was measured with a small overall uncertainty (for example ^{57,58}Sc). However, the division of

the yields of $^{54-56}$Sc measured with the tungsten target and a stripper between the two target materials was very uncertain. In addition, reliable lower limits could not be established for the two interesting isotopes ^{40}Al and ^{67}Mn owing to large uncertainties in the transmission. The cross sections for the production of some other isotopes (e.g., ^{51}Cl and ^{56}K) with the beryllium targets, needed to correct the measured cross sections with the tungsten target, had to be extrapolated. Finally, the cross sections needed for the correction of the data with the carbon stripper (data set 9 in Table II) were calculated by normalizing the beryllium cross sections by the ratio of the total reaction cross sections $\sigma_C/\sigma_{Be} = 1.05$ from the EPAX parametrization.

The compilation of results in Fig. 8 clearly shows a larger (sometimes exceeding a factor of 10) cross section with the tungsten target for the production of very neutron-rich isotopes of the elements $16 \leqslant Z \leqslant 25$ at this projectile energy. The geometrical factor (based on EPAX) is only 1.9. Similarly, large ratios were recently obtained with a ^{48}Ca primary beam at a very similar beam energy [8]. Models of nuclear reactions used for counting rate estimates, such as the intranuclear-cascade plus evaporation model [25] or abrasion-ablation in LISE^{++} [26], do not reproduce the low yields of exotic nuclei observed in this work. The predictions of the EPAX parametrization for reactions with beryllium, shown by the solid lines in Fig. 8, reproduce the measured cross sections rather well in the region $13 \leqslant Z \leqslant 16$. The data for the elements with $Z > 16$ generally fall below the predicted values but have a similar slope.

C. Q_g systematics

The production cross sections for the most neutron-rich projectile fragments have been previously shown to have an exponential dependance on Q_g (the difference in mass excess of the beam particle and the observed fragment) [8,12]. However, it is important to note that the actual masses of the very neutron-rich nuclei, needed for this calculation, have not been measured and are only available from models. There are many differences among mass models; therefore deviations from the predicted yield using a given mass model might be able to identify missing features in that mass model. For example, significant deviations of the real masses can be expected from the model predictions if a new island of inversion near ^{62}Ti [11] (similar to the island of inversion observed near ^{31}Na) is present but is omitted from the models. In a shell-model picture, the ground states of nuclei in the new island of inversion would be dominated by intruder configurations corresponding to neutron particle-hole excitations across the $N = 40$ subshell gap into the $g_{9/2}$ [11]. As a test of this suggestion, the cross sections for the production of all nuclei observed with the beryllium and tungsten targets are shown in Fig. 9 where the abscissa, Q_g, is the difference between the mass of the ground state of the projectile and the observed fragment. In this case the masses were taken from Ref. [10]. This empirical mass model (KTUY) provides an excellent systematization of the variation of the data, with the logarithm of the cross sections for each isotopic chain falling on an approximately straight line.
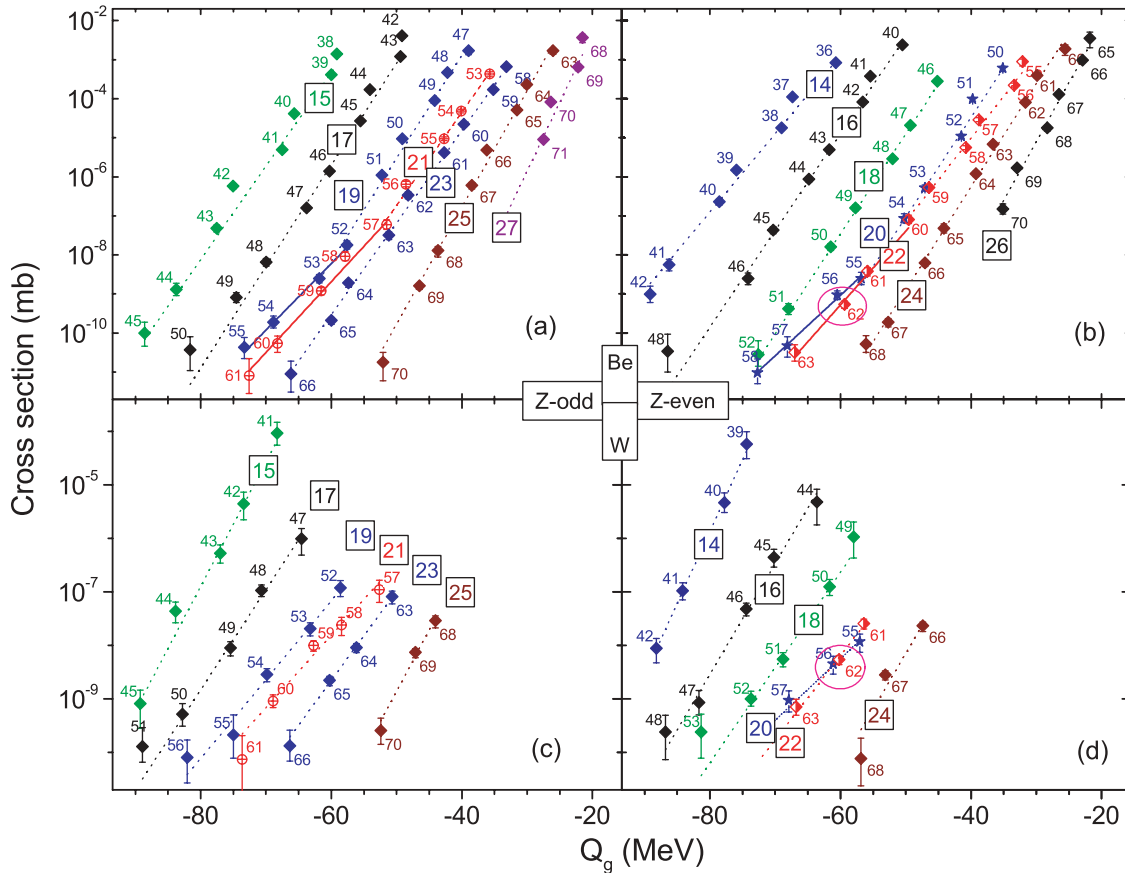
FIG. 9. (Color online) Cross sections for the production of neutron-rich nuclei with (a, c) odd atomic numbers and (b, d) even atomic numbers, with (a, b) a beryllium target [12] and (c, d) a tungsten target, respectively. See text for explanation of Q_g and the lines. The cross sections for ^{62}Ti at the center of the proposed new island of inversion [11] are circled.

The cross sections for each isotopic chain were fitted with the simple expression

$$\sigma(Z, A) = f(Z) \exp(Q_g/T), \tag{3}$$

where T is an effective temperature extracted from the slope. Nearly all the data from the beryllium targets can be fitted with the single value of $T = 1.8$ MeV, but slightly better fits are obtained by finding the optimum T for each element. However, the heaviest isotopes of elements in the middle of the distribution ($Z = 19, 20, 21,$ and 22) appear to break away from the straight-line behavior. These heaviest four or five isotopes of these elements were found to have a shallower slope (shown by the solid lines) or enhanced cross sections relative to the model prediction.

The systematic variation of the production cross sections as a function of Q_g was checked with several other well-known mass models and essentially the same behavior was observed. Note that the differences among the mass models are small compared to the abscissa in Fig. 9. Specifically, models based on the Hartree-Fock-Bogoliubov method, HFB-8, HFB-9 [27], and the very recent HFB-17 version [28], the finite range droplet model (FRDM) [29], and the 2003 Atomic Mass Evaluation (AME2003) [30] with shell-crossing corrections that were developed in the LISE^{++} framework [31] were found to give similar results.

The different behavior of the calcium isotopes with the beryllium target can be seen more clearly in Fig. 10. The same
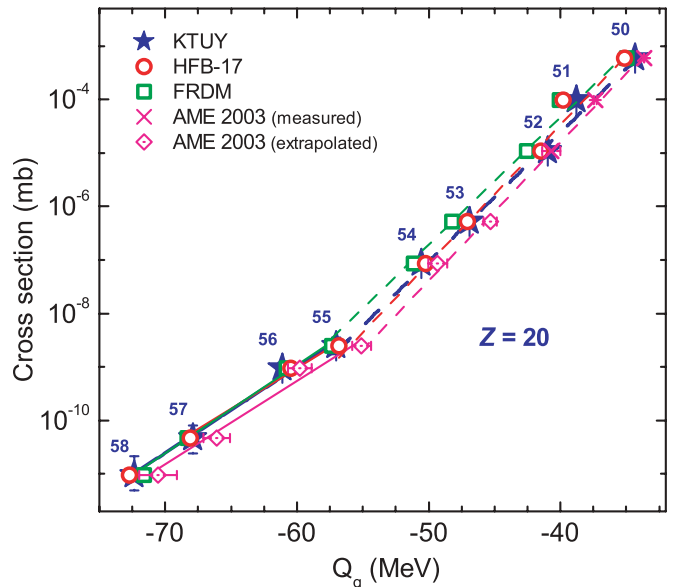

FIG. 10. (Color online) Production cross sections of neutron-rich calcium isotopes with a beryllium target as a function of Q_g calculated with different mass models (see text).
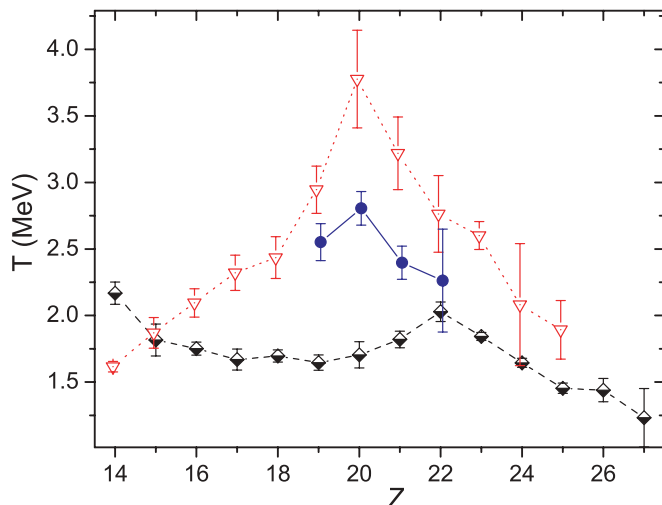
FIG. 11. (Color online) Values of the inverse slope parameter, T, from the best fit of Eq. (3) to the experimental cross sections in Fig. 9 shown as a function of atomic number. Open triangles connected by dotted lines are from the tungsten target, half-filled diamonds connected by dashed lines are from the beryllium target, and the filled circles connected by solid lines are from the heaviest isotopes from the beryllium target in Fig. 9.

effect is present in the same mass region with the tungsten target.

The variation of the individual fitted values of the inverse slope parameter, T, for products from both targets is shown as a function of atomic number in Fig. 11. The inverse slopes of the cross sections from the beryllium target connected by dashed (solid) lines in Fig. 9 are indicated by the half-filled black diamonds and dashed lines (the filled circles and solid lines) in Fig. 11. Similar for the tungsten target the inverse slopes of the measured cross sections are shown by the open red triangles connected by dotted lines in Fig. 11, but the range of cross sections was more limited and only one slope parameter was fitted to their data. Figure 9 clearly shows that there is a general increase in T for all of the heavy isotopes observed with $Z = 19$, 20, 21, and 22.

One possible explanation for the shallower slope of the heaviest nuclei of these isotopes is that these nuclei are more bound (i.e., have less negative Q_g) than predicted by the mass models. A source of stronger binding can be deformation. In a shell-model framework, the wave functions of the ground and low-lying excited states of nuclei in the new island of inversion around ^{62}Ti would be dominated by neutron particle-hole intruder excitations across the $N = 40$ subshell gap, leading to deformation and shape coexistence. Thus, mass measurements of these nuclei, although difficult, would be especially interesting.

V. SUMMARY

The present study of the fragmentation of a ^{76}Ge beam at 132 MeV/u provided evidence for the production of 15 previously unobserved neutron-rich isotopes [12]. The momentum

distributions and cross sections for a large number of neutron-rich nuclei produced by the ^{76}Ge beam were measured by varying the target thickness in a two-stage fragment separator with a fixed momentum acceptance. The longitudinal momentum distributions of 34 neutron-rich isotopes of the elements with $13 \leqslant Z \leqslant 27$ were compared to models that describe the shape and centroid of fragment momentum distributions. New parameters for the semiempirical momentum distribution model [19] based on the measured momenta were obtained. The production cross sections support the previous analysis on the basis of the Q_g function but the most neutron-rich nuclei of elements with $Z = 19$ to 22 are produced with an enhanced rate compared to the systematics. This trend was previously reported for fragmentation on a beryllium target [12] and was found to also be present with the tungsten target. The enhanced yields lie in the region that was previously predicted to be a new island of inversion in which an intruder shell-model state becomes the ground state.

APPENDIX: IDENTIFICATION OF HEAVY IONS WITH ENERGY LOSSES

The magnetic rigidity ($B\rho$) of each particle was obtained by combining an angle measurement provided by two PPACs in the dispersive plane of the S800 analysis beam line in combination with NMR measurements of the dipole fields: $B\rho = B\rho_0(1 + \delta)$, where $B\rho_0$ is the magnetic rigidity of the dipole at the central axis and $\delta = \Delta p/p$ is the fractional deviation of the particle from the central rigidity (for a constant charge q). The mass-to-charge ratio A/q is given by the expression

$$A/q = \frac{B\rho}{\beta\gamma}\frac{e}{uc}, \tag{A1}$$

where e is the elementary charge, u is the atomic mass unit, β is the velocity of the ion relative to the speed of light, c, and γ is the Lorentz factor. The velocity of the ions was determined from the time of flight (TOF). However, for the TOF measurement between the A1900 focal-plane scintillator and the second PIN detector (see Table I and Fig. 2), there were several materials in the path of the beam, leading to different ion velocities along the beam line. To calculate the A/q ratio in this case with Eq. (A1), it was necessary to introduce a reduced $B\rho_a$ value that corresponds to the average velocity $\beta_{ave} = L/(cT)$, where T is the TOF between two timing detectors. The TOF value T can be written as $T = \sum_i^N L_i/(c\beta_i)$, where N is the number of stages where the ion velocity changed owing to the passage through material and L_i is the corresponding flight path at a given velocity.

At intermediate beam energies when the ion's velocity is not significantly changed along the path (e.g., only thin materials are inserted in the beam) one can use the reduced magnetic rigidity as

$$B\rho_a = kL \Big/ \sum_i^N (L_i / B\rho_{0i}),$$

$$(A2)$$

where k is the momentum deviation measured before the last flight stage and $B\rho_{0i}$ is the magnetic rigidity corresponding to the ith stage on the optical axis. At these energies ($\beta = 0.4$) it is possible to omit the γ factor in Eq. (A1) because the ratio of $(\delta\beta/\beta)/(\delta\gamma/\gamma) = 5.2$, whereas it is equal to 1.0 at $\beta = 0.71$.

Calculations using Eq. (A2) for ^{58}Ca fragments (data set 13; see Table II) with the TOF measured between the FP scintillator and the second PIN detector (see Table I) were compared to LISE^{++} Monte Carlo simulations. A maximum difference of $d\beta = 0.06\%$ occurs for ions farthest from the central rigidity ($\Delta p/p = 2.5\%$). This results in a mass resolution for ^{58}Ca of about 0.04 units.

The charge state (q) of the ion was evaluated with a relation based on the total kinetic energy (TKE), velocity, and magnetic rigidity:

$$q = \frac{\text{TKE}}{u(\gamma - 1)(A/q)},$$

$$(A3)$$

where TKE is calculated as a sum of the energy loss values in each of the Si detectors. The velocity before the Si telescope was calculated from the reduced magnetic rigidity and the central magnetic rigidity of the last dipole in the beam line ($B\rho_{0f}$):

$$\beta = \frac{k\beta_{\text{ave}} B\rho_{0f}}{B\rho_a}.$$

$$(A4)$$

The atomic number was determined from the combination of energy loss (ΔE) and velocity values according to the Bethe formula

$$Z \approx \sqrt{\frac{\Delta E}{[\text{MeV}]} \left(\frac{1}{\beta^2} \log \frac{5930}{1/\beta^2 - 1} - 1 \right)}.$$

$$(A5)$$

[1] H. Breuer *et al.*, Phys. Rev. C **22**, 2454 (1980).

[2] D. Guillemaud-Mueller *et al.*, Z. Phys. A **322**, 415 (1985).

[3] M. Weber *et al.*, Z. Phys. A **343**, 67 (1992).

[4] M. Bernas *et al.*, Phys. Lett. **B415**, 111 (1997).

[5] M. Langevin *et al.*, Phys. Lett. **B130**, 251 (1983).

[6] G. G. Adamian, N. V. Antonenko, S. M. Lukyanov, and Y. E. Penionzhkevich, Phys. Rev. C **78**, 024613 (2008).

[7] T. Baumann *et al.*, Nature (London) **449**, 1022 (2007).

[8] O. B. Tarasov *et al.*, Phys. Rev. C **75**, 064613 (2007).

[9] P. F. Mantica *et al.*, Bull. Am. Phys. Soc. **53**, 64 (2008).

[10] H. Koura, T. Tachibana, M. Uno, and M. Yamada, Prog. Theor. Phys. **113**, 305 (2005).

[11] B. A. Brown, Prog. Part. Nucl. Phys. **47**, 517 (2001).

[12] O. B. Tarasov *et al.*, Phys. Rev. Lett. **102**, 142501 (2009).

[13] D. J. Morrissey, B. M. Sherrill, M. Steiner, A. Stolz, and I. Wiedenhöver, Nucl. Instrum. Methods Phys. Res. B **204**, 90 (2003).

[14] D. Bazin, J. Caggiano, B. M. Sherrill, J. Yurkon, and A. Zeller, Nucl. Instrum. Methods B **204**, 629 (2003).

[15] R. Grzywacz *et al.*, Phys. Lett. **B355**, 439 (1995).

[16] O. B. Tarasov and D. Bazin, Nucl. Instrum. Methods B **266**, 4657 (2008), http:\\www.nscl.msu.edu\lise.

[17] M. Lewitowicz *et al.*, Z. Phys. A **335**, 117 (1990).

[18] A. S. Goldhaber, Phys. Lett. **B53**, 306 (1974).

[19] D. J. Morrissey, Phys. Rev. C **39**, 460 (1989).

[20] R. Pfaff *et al.*, Phys. Rev. C **51**, 1348 (1995).

[21] O. Tarasov, Nucl. Phys. **A734**, 536 (2004).

[22] M. Fauerbach, D. J. Morrissey, W. Benenson, B. A. Brown, M. Hellström, J. H. Kelley, R. A. Kryger, R. Pfaff, C. F. Powell, and B. M. Sherrill, Phys. Rev. C **53**, 647 (1996).

[23] O. B. Tarasov *et al.*, Nucl. Instrum. Methods Phys. Res. A (to be submitted).

[24] K. Sümmerer and B. Blank, Phys. Rev. C **61**, 034607 (2000).

[25] D. J. Morrissey, L. F. Oliveira, J. O. Rasmussen, G. T. Seaborg, Y. Yariv, and Z. Fraenkel, Phys. Rev. Lett. **43**, 1139 (1979).

[26] O. B. Tarasov and D. Bazin, Nucl. Instrum. Methods B **204**, 174 (2003).

[27] M. Samyn, S. Goriely, and J. M. Pearson, Nucl. Phys. **A725**, 69 (2003).

[28] S. Goriely, N. Chamel, and J. M. Pearson, Phys. Rev. Lett. **102**, 152503 (2009).

[29] P. Möller, J. R. Nix, W. D. Myers, and W. J. Swiatecki, At. Data Nucl. Data Tables **59**, 185 (1995).

[30] G. Audi, A. H. Wapstra, and C. Thibault, Nucl. Phys. **A729**, 337 (2003).

[31] O. B. Tarasov and D. Bazin, Tech. Rep. MSUCL1248, NSCL, MSU, 2002.